The Maxey-Riley-Gatignol equations for macroplastics in the North West European Shelf region

Meike F. Bos[1], Irina I. Rypina[2], Larry J. Pratt[2], and Erik van Sebille[1]

[1]Institute for Marine and Atmospheric Research, Utrecht University, Netherlands
[2]Woods Hole Oceanographic Institution, Woods Hole, USA

Correspondence: Meike F. Bos (m.f.bos@uu.nl)

Abstract. Floating macroplastics in the ocean have a finite size and density lower than the water in which they are drifting. Due to their inertia, they do not perfectly follow the ocean currents, and their motion might be better described by the Maxey-Riley-Gatignol equations. In this work, we tailor these equations to simulate fully submerged buoyant macroplastics moving in 2D in the North West European shelf Region, where the flow is highly variable in space and time. We implement the Maxey-Riley-Gatignol equations in the Lagrangian simulation framework Parcels. For macroplastics in the North West European shelf we need a particle Reynolds number dependent drag force as we find particle Reynolds numbers of order 100 and thus beyond the Stokes regime. We show that for these higher particle Reynolds numbers, we can ignore the history force and use the slow manifold Maxey-Riley-Gatignol equations. Using these equations to study the trajectories of buoyant macroplastics in the North West European shelf, we find that higher particle Reynolds numbers make the macroplastic trajectories more similar to tracer particles. The difference between tracer particles and macroplastic particles advected with the Maxey-Riley-Gatignol equations is mainly caused by the forcing associated with the Coriolis effect, whereas the forcing associated with the gradients in the velocity field has only a minor effect. This work is a first step towards including inertial effects in Lagrangian simulations of macroplastics in coastal regions with highly varying velocity fields.

1 Introduction

Macroplastics make up most of the mass of plastic in the ocean (Eriksen et al., 2014; Kaandorp et al., 2023). Most plastic enters the ocean in the form of macroplastics (Morales-Caselles et al., 2021) to only later fragment into microplastics. Thus, cleaning up macroplastic is potentially an effective way to prevent microplastic pollution in the ocean. However, the distribution of macroplastic varies widely in space and time (Morales-Caselles et al., 2021), especially in coastal regions where most macroplastic enters the ocean (Tekman et al., 2022). What processes cause this large variability is not yet understood. In our study, we investigate how inertia, added mass, and other effects that distinguish the motion of a rigid particle from a fluid element, affect the trajectories of macroplastics.

Most commonly in Lagrangian analysis, plastic particles are advected with the fluid flow (Lebreton et al., 2012; Kaandorp et al., 2023; Liubartseva et al., 2018). For buoyant plastics at the ocean surface, 2D surface fluid velocities are often used, sometimes with an additional windage term (Breivik et al., 2011; Maximenko et al., 2018). For plastics in the interior of the

25   ocean, a vertical rising or sinking velocity is often added to the 3D fluid velocities to account for the particle's buoyancy (Soto-Navarro et al., 2020). However, the macroplastics' finite size and density different from the water around them, makes their behavior inherently different from water parcels.

For particles that are much smaller than the typical scales of the flows in which they are embedded, the motion can be described by the Maxey-Riley-Gatignol (MRG) equations, as developed by Maxey and Riley (1983) and Gatignol (1983). The

30   MRG equations use Newtons second law to find the velocity and position of the particle over time. Over the years, the MRG equations have been adjusted to also include Coriolis effects (Tanga et al., 1996), shape effects (Sunberg et al., 2024) and the effects of winds for buoyant particles (Beron-Vera et al., 2019). The MRG equations are most commonly used for particles smaller than macroplastics (e.g., microplastics), and/or in lab-flows instead of oceanic flows, which have vastly different length and timescales.

35   The MRG equations have already been used to study macro sized objects in the open ocean. Beron-Vera et al. (2019) showed that for undrogued drifter particles with a diameter of 17.5 cm, the MRG equations that include windage effect were able to reproduce the accumulation pattern in the North Atlantic gyre. More recently, Beron-Vera and Miron (2020) proposed an MRG model for (a network of) sargassum plants with a diameter of 10 cm. Bonner et al. (2024) showed that this model was able to reproduce the trapping of sargassum in mesoscale eddies. The concentrations predicted by this model better matched with

40   satellite observations than the concentrations predicted using a leeway model.

As most macroplastic enters the ocean in coastal areas, we want to investigate the effect of the MRG terms on the trajectories of macroplastics in coastal areas. Here we focus on the North-West European shelf (NWES) region, where macroplastics are abundant and where large spatial and temporal variations in their concentration have been observed at both the sea surface and on the beaches (Turrell, 2019; Le Moigne et al., 2021; Tekman et al., 2022). The flow in this region is characterized by an eddy

45   dominated regime off the continental shelf and a wind- and tidal driven regime on the continental shelf (see Ricker and Stanev (2020) and references therein). We use the high resolution NWES ocean model of CopernicusMarineServices with a spatial resolution of $1/36°$ and temporal resolution of 1 hour.

Our work consists of two parts. First, we discuss the form of the MRG equations suitable to simulate macroplastics in the NWES. Second, we use this form of the MRG equation to perform simulations of macroplastics in the NWES and investigate

50   whether the MRG equation affect the particle trajectory compared to surface tracers.

2 Theory

2.1 General form of MRG equations for macroplastics

In its most general form, the MRG equations include the following forces: the drag force, the inertia force (due to the acceleration of the fluid), the added mass force, the buoyancy force, the lift force, Coriolis terms associated with the added mass, fluid

55   motion and centrifugal acceleration and the history force with Coriolis correction. Throughout the paper, we use the subscript p for the particle and subscript f for the fluid. We denote the position using x, velocity using u and time using t. Then, after introducing the particle's buoyancy $B = \rho_p/\rho_f$ as the ratio between the density of the particle and fluid, we can write the MRG

equations for spherical particles as:

$$\frac{d\boldsymbol{x}_p}{dt} = \boldsymbol{u}_p \tag{1}$$

$$\frac{d\boldsymbol{u}_p}{dt} = -\frac{18\nu c(\mathrm{Re}_p)}{Bd^2}(\boldsymbol{u}_p - \boldsymbol{u}_f) + \frac{1}{B}\frac{D\boldsymbol{u}_f}{Dt} + \frac{1}{2B}\left(\frac{D\boldsymbol{u}_f}{Dt} - \frac{d\boldsymbol{u}_p}{dt}\right) + \left(1 - \frac{1}{B}\right)\boldsymbol{g} - \frac{1}{2B}\boldsymbol{\omega}_f \times (\boldsymbol{u}_p - \boldsymbol{u}_f)$$

$$-\frac{1}{2B}\boldsymbol{f} \times (\boldsymbol{u}_p - \boldsymbol{u}_f) + \frac{1}{B}\boldsymbol{f} \times \boldsymbol{u}_f - \boldsymbol{f} \times \boldsymbol{u}_p - \frac{9\sqrt{\nu}}{\sqrt{\pi}Bd}\int_{t_0}^{t} H(t-s)\left(\frac{d}{ds}(\boldsymbol{u}_p(s) - \boldsymbol{u}_f(s)) + \boldsymbol{f} \times (\boldsymbol{u}_p(s) - \boldsymbol{u}_f(s))\right)ds.$$

Here, we have normalized the force balance by the mass of the particle $m_p = \rho_p \pi d^3/6$ where d is particle's diameter. In the equation, D/Dt denotes the material derivative with respect to the fluid flow and ν is the kinematic viscosity. The vorticity of the fluid is given by $\boldsymbol{\omega}_f = \nabla \times \boldsymbol{u}_f$. The Coriolis particle is denoted by $\boldsymbol{f} = 2\Omega \sin\phi \hat{e}_3$ with Ω being the rotation of the earth and ϕ the latitude of the particle. $H(t-s)$ denotes the history kernel, its exact form we will discuss in section 2.3. We set $\mathrm{u}_p(t_0) = \mathrm{u}_f(t_0)$ so that the contribution from the initial velocities to the history term is zero (Farazmand and Haller, 2015). To shorten the notation, we do not explicitly write all the dependencies like $\boldsymbol{u}_{p/f}(\boldsymbol{x}_{p/f}, t)$ and $\mathrm{x}_{p/f}(t)$. In the above equation we ignored Faxen's corrections, as gradients in the velocity field of oceanic flows will be on scales much bigger than the size of typical macroplastics. We use a generalized expression for the drag force by employing the drag correction function $c(\mathrm{Re}_p)$ for nonzero particle Reynolds number, where the particle Reynolds number is defined as:

$$\mathrm{Re}_p = \frac{|\boldsymbol{u}_{\mathrm{slip}}|d}{\nu}, \tag{2}$$

with the slip velocity given by $\boldsymbol{u}_{\mathrm{slip}} = \boldsymbol{u}_p - \boldsymbol{u}_f$. In section 2.2 we discuss the exact form $c(\mathrm{Re}_p)$ and its effect on the drag force. The added mass force is independent of the particles' Reynolds number (Mei et al., 1991; Kim et al., 1998). Its functional form depends only on the geometry of the object (Wakaba and Balachandar, 2007). Rearranging Eq. (1) allows us to solve for $\frac{d\boldsymbol{u}_p}{dt}$:

$$\frac{d\boldsymbol{u}_p}{dt} = -\frac{c(\mathrm{Re}_p)}{\tau_s}(\boldsymbol{u}_p - \boldsymbol{u}_f) + \frac{3}{1+2B}\left(\frac{D\boldsymbol{u}_f}{Dt} - (\boldsymbol{f} + \boldsymbol{\omega}_f) \times (\boldsymbol{u}_p - \boldsymbol{u}_f)\right) + \frac{2(1-B)}{1+2B}(\boldsymbol{f} \times \boldsymbol{u}_p - \boldsymbol{g}) \tag{3}$$

$$-\frac{3}{\sqrt{\pi(1+2B)\tau_s}}\int_{t_0}^{t} H(t-s)\left(\frac{d}{ds}(\boldsymbol{u}_p(s) - \boldsymbol{u}_f(s)) + \boldsymbol{f} \times (\boldsymbol{u}_p(s) - \boldsymbol{u}_f(s))\right)ds$$

where we introduced the Stokes relaxation time

$$\tau_s = \frac{d^2(1+2B)}{36\nu}. \tag{4}$$

In this study, we will use a typical (spherical) macroplastic particle with a diameter of 25 cm and a buoyancy of $B = 0.68$. These values are based on the properties of MetOcean Stokes drifters (Wienders, 2021). For seawater we use a density of 1027 kg/m^3 and dynamic viscosity of $1.32 \cdot 10^{-3}$ Pa·s, corresponding to the average salinity of 34.7 g/kg and average temperature of 12° C (Sharqawy et al., 2010). The averages were taken over the NWES domain and simulation period considered in this work. For these values we find $\tau_s = 3196\,\mathrm{s} \approx 53$ min.

2.2 Drag Force

85 In the original MRG formalism, it is assumed that the drag force is given by Stokes drag:

$$F_{\mathrm{drag}}^{\mathrm{Stokes}} = -3\pi\nu\rho_f d(\boldsymbol{u}_p - \boldsymbol{u}_f). \tag{5}$$

In principle, the type of drag force the particle experiences depends on the particle's Reynolds number as defined in Eq. (2). As the particle's Reynolds number scales with the size of the particle, the type of drag force may change too.

For the drag force, there is a crossover regime from Stokes drag at $\mathrm{Re}_p < 1$ to Newtonian drag that is proportional to the
90 square of the slip velocity at $\mathrm{Re}_p > 10^3 - 10^6$ (Dey et al., 2019). In the transitional range between these two regimes, the exact form of the drag force is a function of the particle Reynolds number. There exist several empirical expressions for the drag force in this transient regime (Dey et al., 2019). We use the drag correction function as proposed by White (1991), valid for $0 \le \mathrm{Re}_p < 10^5$, which is given by:

$$c(\mathrm{Re}_p) = 1 + \frac{\mathrm{Re}_p}{4\left(1 + \sqrt{\mathrm{Re}_p}\right)} + \frac{\mathrm{Re}_p}{60}. \tag{6}$$

95 From this equation we can see that the drag correction function, and thus the drag force, increases with increasing particle Reynolds number. This will in turn affect the particle Reynolds number, as an increasing drag force will result in a lower slip velocity and thus in lower Reynolds numbers.

As we have a heterogeneous velocity field, we do not know the particle Reynolds number apriori. Here, as first estimate for particle Reynolds numbers in our system we assume a simple geostatic flow given by $\boldsymbol{u}_f = (U, 0)$. We can find an analytical
100 expression for the steady state slip velocity from Eq. (3) without history term. The horizontal u and v component of the steady state slip velocity are given by:

$$u_{\mathrm{slip}} = \frac{2(1-B)\tau_s^2 f^2}{(1+2B)(c(\mathrm{Re}_p)^2 + \tau_s^2 f^2)} U, \tag{7}$$

$$v_{\mathrm{slip}} = \frac{2(1-B)c(\mathrm{Re}_p)\tau_s f}{(1+2B)(c(\mathrm{Re}_p)^2 + \tau_s^2 f^2)} U. \tag{8}$$

We can use these components to calculate Re_p using Eq. (2). If we use a typical tidal flow velocity of $U = 1$ m/s, we can
105 numerically solve this equation for Re_p. For this value of U we find $\mathrm{Re}_p = 867$, which corresponds to a drag correction factor of $c(876) = 23$, which is clearly outside the Stokes regime.

In addition, as the flow velocities in the NWES change in space and time, it is expected that drag regime experienced by the particle is not constant as well. We therefore explore the possibility to have a particle specific drag correction factor $c_p(t)$ that changes over time, as was already proposed by Mei and Adrian (1992) and used more recently by AlAli et al. (2024). In
110 section 4.1, we perform sensitivity simulations to find typical values for the particle Reynolds number of macroplastics in the NWES and study its variation in time and space to find what values to use for the drag correction factor.

In reality, buoyant particles will partly stick out of the surface and thus not only experience a drag force due to the ocean flow but also a drag force due to the wind. Beron-Vera et al. (2019) developed an extension to the MRG equations (the BOM-equations), that captured both the contribution from the water and air drag on the particle as function of the buoyancy of

115 the particle. The formulation of the BOM equations assumes Stokes drag for both water and air, whereas particle Reynolds numbers for macroplastic in the NWES can be larger than in the Stokes regime. In principle, the BOM equations could be modified to include generalized $c(\mathrm{Re}_p)$-dependent drag forces acting on the submerged and sticking out parts of the particle, with different drag correction values for ocean and atmosphere. In the current work, we ignore the drag force exerted by the wind, and instead focus on particles that are completely submerged in the ocean. This allows us to better understand how

120 macroplastics couple to oceanic flow characteristics through the MRG equations.

2.3 History Force

The history force represents the effect of the evolving and temporarily delayed boundary layer around the particle as its slip velocity changes. Daitche (2015) and Urizarna-Carasa et al. (2025) have shown that the history force can significantly alter the trajectories of particles, making them more flow-following. The history term makes the MRG equations integral-differential

125 equations and thus computationally expensive to solve. Hence, the term is often ignored based on the complexity of solving the MRG equations when using this term, rather than on physical arguments.

The history force is given by

$$\boldsymbol{F}_{\text{history}} = -\frac{3}{2}\rho_f\sqrt{\pi\nu}d^2\int\limits_{t_0}^{t}H(t-s)\left(\frac{d}{ds}(\boldsymbol{u}_f(s)-\boldsymbol{u}_p(s))+\boldsymbol{f}\times(\boldsymbol{u}_f(s)-\boldsymbol{u}_p(s))\right)ds. \tag{9}$$

$H(t-s)$ denotes the history kernel, the exact form of which depends on the particle Reynolds number Re_p. In a purely viscous

130 flow ($\mathrm{Re}_p = 0$), the history kernel is given by the Basset kernel:

$$H_{\text{Basset}}(t-s) = \frac{1}{\sqrt{t-s}}. \tag{10}$$

However, for systems with a nonzero Re_p, the Basset kernel overestimates the history force. Sano (1981) studied the drag on a sphere that experienced a sudden initial acceleration. He showed that the drag force decayed at short timescales with $t^{-1/2}$, as given by the Basset kernel, but on longer timescales the drag force decayed as t^{-2}. This faster decay at long timescales

135 is associated with Oseen convective inertia effects, where once the vorticity around the sphere moves out of the diffusive boundary layer it is transported by convection in the wake region behind the particle. Lovalenti and Brady (1993) extended the derivation of Sano (1981) for a sphere with arbitrary time-dependent motion. They introduced the Oseen timescale $t_O = \nu/u_{\text{slip}}^2$ as timescale beyond which the t^{-2} decay is found. In general, there are two timescales associated with the history term: (i) the diffusive timescale t_d and (ii) the Oseen time t_O (Jaganathan et al., 2023). The diffusive timescale is defined as the time

140 it takes for a fluid molecule to diffusive over the length over the particle: $t_d = d^2/\nu$. The Oseen time is defined as the time it takes for a water parcel to be transported a distance d_O away from the particle, where d_O is the distance beyond which $\mathrm{Re}_p^O = |\boldsymbol{u}_{\text{slip}}|d_O/\nu > 1$. For small Reynolds numbers and/or particles starting from a zero slip velocity there is a regime where $t_d < t_O$ and the Basset history term is a good approximation. Mei and Adrian (1992) used the results of numerical simulations to propose a semi-empirical history kernel for nonzero Re_p that decays as the Basset kernel on short times and as t^{-2} over long

145 times. This kernel is given by:

$$H_{\text{Mei/Adrian}}(t-s,c_1,c_2) = \left[(t-s)^{1/(2c_1)} + \left(\frac{2\nu\sqrt{\nu\pi}(t-s)^2}{((f_H(s))^3 d^3}(\text{Re}_p(s))^3 \right)^{1/c_1} \right]^{-c_1} \qquad \text{with} \qquad (11)$$

$$f_H(s) = \frac{3}{4} + c_2 \text{Re}_p(s).$$

Their original work was tested for a flow over a stationary sphere, where the flow had small fluctuations in the free-stream velocity. They studied systems with $Re_p \in [0.1, 100]$ and found $c_1 = 2$ and $c_2 = 0.105$. Kim et al. (1998) tested the Mei/Adrian

150 history kernel for a freely moving sphere injected into an initially stationary or oscillating fluid with $\text{Re}_p \in [2, 150]$. They found $c_1 = 2.5$ and $c_2 = 0.126$. Dorgan and Loth (2007) fitted the kernel to experimental data of settling spheres. They used the constant terminal velocity to calculate the $\text{Re}_{p,\text{term}}$, which is larger than the instantaneous particle Reynolds number a particle experiences when it is released from rest. They used data with $\text{Re}_{p,\text{term}} \in [6.5, 853]$ and found $c_1 = 2.5$ and $c_2 = 0.2$. The systems for which the Mei/Adrian kernel was developed and tested differ in three ways from our system of macroplastics

155 in oceanic flows. Firstly, the Mei/Adrian kernel has not been tested for flexible $c_p(t)$. Secondly, the Mei/Adrian kernel has only been tested for sinking particles, *i.e.* $B > 1$. Thirdly, the Mei/Adrian kernel was developed for microscopic particles and thus using macroscopic particles leads to cross-over times at which the t^{-2} decay dominates over the $t^{-1/2}$ decay in the history kernel much larger than the Oseen time. This can be seen by defining a cross-over timescale of the kernel where the first and the second term in Eq. 11 exactly balance each other:

160 $$t_{\text{Mei/Adrian}} = \left(\frac{4}{\pi} \right)^{1/3} \left(\frac{3}{4}\sqrt{t_O} + c_2\sqrt{t_d} \right)^2 . \qquad (12)$$

As the diffusion time t_d increases with increasing particle size, so does this cross-over time. If we compare the diffusion time, Oseen time and the cross-over time for a particle of $d = 25$ cm with Re_p and $|\boldsymbol{u}_{\text{slip}}|$ as found using geostatic balance (Eqs. (7) and (8)), we find that there is a difference of multiple orders of magnitude between the timescales: $t_d = 5 \cdot 10^4$ s, $t_{\text{Mei/Adrian}} = 5 \cdot 10^2$ s and $t_O = 6 \cdot 10^{-2}$ s. While for a particle with a diameter of 2.5 cm we find that the timescales are on the

165 same order: $t_d = 13$ s, $t_{\text{Mei/Adrian}} = 15$ s and $t_O = 4$ s.

The large difference between the cross-over time, diffusion time and Oseen time for macroscopic particles raises the question whether the Mei/Adrian kernel can be used for our system or whether a window-based approach with the Oseen time is more appropriate. As there is no validated functional form of the history force for our system, we do not implement it in our simulations. Instead, we use the measured slip velocities of the particles in simulations to estimate its magnitude without

170 implementing its effect. In section 4.2, we calculate the magnitude of the history term using the Mei/Adrian kernel and using the Basset kernel integrated over the Oseen time and compare its magnitude to the other terms in the MRG equations.

When calculating the Mei/Adrian history term numerically, we need to account for the singularity at the upper bound of the integral, which means that one cannot take a simple Riemann summation. Several methods exist for calculating the history term numerically, as described in the reviews by Moreno-Casas and Bombardelli (2016) and Jaganathan et al. (2023). We use

175 the trapezoidal-based method developed by van Hinsberg et al. (2011), this method uses a window approach where the history force is calculated over a finite time window where it is assumed that the contributions before $t - t_{\text{window}}$ are so small that they

can be ignored. Depending on the timescales involved in the system, one might need large t_{window}, which results in a large memory demand. To circumvent this, Prasath et al. (2019) proposed a different method. They solve the Basset history force by reformulating the problem in such that the MRG equation is a dynamic boundary condition for a 1D diffusion equation. With their formulation, the memory demand does not increase with time. Their method is strictly valid for $\text{Re}_p = 0$ or on timescales $t < t_O$ as they use the Basset history kernel.

2.4 Slow manifold MRG equation

For the case that the drag force dominates and the history term can be ignored, the MRG equations can be simplified to the slow manifold (SM) MRG equation. For a complete derivation, see the work of Haller and Sapsis (2008). The general idea is to non-dimensionalize the MRG equations by introducing a typical velocity of the flow U and typical length scale of the fluid flow L. In doing so one can define the dimensionless Stokes number $\varepsilon = \tau_s \frac{U}{L}$ and dimensionless position $\boldsymbol{X} = \boldsymbol{x}/L$, time $\tau = tU/L$, velocities $\boldsymbol{U} = \boldsymbol{u}/U$, Coriolis parameter $\boldsymbol{\mathcal{F}} = \boldsymbol{f}L/U$, vertical fluid vorticity $\boldsymbol{\Omega}_f = \boldsymbol{\omega}_f L/U$ and gravitational acceleration $\boldsymbol{G} = \boldsymbol{g}L/U^2$. Using these definitions, the dimensionless form of the MRG equations are given by

$$
\frac{d\boldsymbol{X}_p}{d\tau} = \boldsymbol{U}_p,
$$
$$
\frac{d\boldsymbol{U}_p}{d\tau} = -\frac{c(\text{Re}_p)}{\varepsilon}\left(\boldsymbol{U}_p - \boldsymbol{U}_f\right) + \frac{3}{1+2B}\left(\frac{D\boldsymbol{U}_f}{D\tau} - (\boldsymbol{\mathcal{F}} + \boldsymbol{\Omega}_f)\times(\boldsymbol{U}_p - \boldsymbol{U}_f)\right) + \frac{2(1-B)}{1+2B}(\boldsymbol{\mathcal{F}}\times\boldsymbol{U}_p - \boldsymbol{G}) \tag{13}
$$
$$
-\frac{3}{\sqrt{\pi(1+2B)\varepsilon}}\int_{\tau_0}^{\tau}\mathcal{H}(\tau-\sigma)\left(\frac{d}{d\sigma}(\boldsymbol{U}_p - \boldsymbol{U}_f) + \boldsymbol{\mathcal{F}}\times(\boldsymbol{U}_p - \boldsymbol{U}_f)\right)d\sigma
$$

Here $\mathcal{H}(\tau - \sigma)$ is the rescaled history kernel, *i.e.* where t and s are replaced by their dimensionless counterparts. If we ignore the history force we can find the slow manifold reduction up to first order in ε. We come back to the assumption of a negligible history force in Section 4.2 where we investigate its magnitude in our system. In a system with Stokes drag ($c(0) = 1$), the slow manifold reduction is traditionally achieved through an asymptotic expansion in the Stokes number ε. For *fixed* $c(\text{Re}_p^{\text{In}}) > 1$ the slow manifold reduction can easily be achieved by expanding in $\tilde{\varepsilon} = \varepsilon/c(\text{Re}_p^{\text{In}})$ instead of ε. For *flexible* $c_p(t)$ the drag correction factor, and therefore $\tilde{\varepsilon}$, become functions of dependent variable $\boldsymbol{U}_f - \boldsymbol{U}_p$ and $\tilde{\varepsilon}$ is no longer a fixed parameter. However, an extension of the slow manifold reduction can still be made using the traditional Stokes number ε. For $d = 25$ cm, $U \sim 1$ m/s and $L = 10$ km (typical displacement by the tides) we find $\varepsilon = 0.32 < 1$ and thus ε can be used as the (moderately) small parameter. An expansion of the form

$$
\boldsymbol{U}_p = \boldsymbol{U}_f + \varepsilon\boldsymbol{U}_p^{(1)} + \mathcal{O}(\varepsilon^2) \tag{14}
$$

will recover the $\mathcal{O}(\varepsilon)$ slow manifold reduction in the form

$$
\frac{d\boldsymbol{X}_p}{d\tau} = \boldsymbol{U}_p = \boldsymbol{U}_f + \frac{\varepsilon}{c(\text{Re}_p)}\frac{2(1-B)}{1+2B}\left(\frac{D\boldsymbol{U}_f}{D\tau} + \boldsymbol{\mathcal{F}}\times\boldsymbol{U}_f - \boldsymbol{G}\right) + \mathcal{O}(\varepsilon^2). \tag{15}
$$

Several caveats apply. First, if the expansion is carried to $\mathcal{O}(\varepsilon^2)$, complications will emerge from the dependence of $c(\text{Re}_p)$ upon $\boldsymbol{U}_f - \boldsymbol{U}_p$. Second, the expansion in ε is a singular perturbation and, as such, produces a solution that is incapable of

satisfying a full set of initial conditions. In the absence of the history term, it can be shown (Haller and Sapsis, 2008) that a solution satisfying arbitrary initial conditions will tend toward the slow manifold exponentially rapidly. An explicit solution was written down in Rypina et al. (2024). With the history term included, it can be shown that relaxation still occurs, but at a rate that is algebraic rather than exponential (Langlois et al., 2015). These results formally hold for small Stokes number.

210 After redimensionalizing Eq (15), we find the following form of the SM-MRG equation:

$$\frac{d\boldsymbol{x}_p}{dt} = \boldsymbol{u}_p = \boldsymbol{u}_f + \frac{\tau_s}{c(\mathrm{Re}_p)} \frac{2(1-B)}{1+2B} \left(\frac{D\boldsymbol{u}_f}{Dt} + \boldsymbol{f} \times \boldsymbol{u}_f - \boldsymbol{g} \right). \tag{16}$$

The SM-MRG equation reveals that the particle velocity is given by the fluid velocity and a correction term. When this correction term is negligible, we end up with the passive tracer equation normally used in Lagrangian simulations: $\frac{d\boldsymbol{x}_p}{dt} = \boldsymbol{u}_f$.

When the SM-MRG is valid, it is beneficial to perform Lagrangian simulations with this equation rather than with the MRG

215 equation (Eq. (3)). Using the SM-MRG equation speeds up the simulation, as there is no need to solve for the acceleration of the particle. In addition, the algorithm with the SM-MRG equation is more stable, allowing to use bigger integration timesteps. This is because the drag force in the MRG equations scales with $c(\mathrm{Re}_p)/\tau_s$. This term becomes big for large Re_p, and thus we need a small timestep to have $c(\mathrm{Re}_p)\mathrm{dt}/\tau_s \lesssim 1$, which is needed to keep the numerical integration stable.

Whether the SM-MRG equation and MRG equations give the same results has to be tested carefully. Rypina et al. (2024)

220 showed that for particles in 3D vortex flows with $\varepsilon = 0.33$, the trajectories of the particles advected with the SM-MRG equation deviated significantly from the trajectories of particles advected with the MRG equations. In section 4.3, we performed sensitivity tests to estimate whether we can use the SM-MRG equations in our system of a 25 cm Stokes-drifter in the NWES, or whether we need the full MRG equations.

3 Methods

225 We used the Parcels framework v.3.0.2 (Delandmeter and van Sebille, 2019) for Lagrangian simulations together with the Atlantic - European North West Shelf (NWES) Ocean Physics Analysis and Forecast (https://doi.org/10.48670/moi-00054) from Copernicus Marine Services. The NWES dataset spans from latitude $46.03°$ N to $61.28°$ N and longitude $16°$ W to $9.97°$ E. It has a grid resolution of $1/36°$ in both the zonal and meridional direction. The data in this dataset is located on a regular A grid (interpolated from the native grid model; a $1/36°$ staggered Arakawa-C grid). The product includes the 11

230 main tidal components and wave forcing, *i.e.*, the Stokes-Coriolis process, the surface stress, and the Turbulent Kinetic Energy (TKE) induced by wave breaking fields. We use the hourly averaged surface velocity fields, located at a depth of about 0.5 m. We used data from 1 September 2023 until 1 March 2024. In addition, to test the effect of the underlying temporal resolution of the field, we used the daily averaged fields at the same depth for the same time period.

3.1 Numerical integration with Parcels

For the advection of tracer particles in Parcels, we use the 4th order Runge-Kutta scheme (RK4), which is a build-in advection kernel in Parcels. We can use the same scheme for advecting the plastic particles with the SM-MRG equation. For this, we wrote a custom Parcels kernel that not only takes into account u_f but also the rest of the terms in Eq. (16).

Parcels loads in flow velocities profiles on a grid and uses interpolation to calculate the fluid velocity at the location of the particle. The velocity is linearly interpolated in both space and time. In general, the model output fields do not contain the spatial and temporal derivatives of fluid velocity. To calculate the material derivative of the fluid field at the location of the particle, we use finite differences in both space and time, *i.e.*:

$$\frac{d\boldsymbol{u}_f}{dx} \approx \frac{\boldsymbol{u}_f(x+\delta x) - \boldsymbol{u}_f(x-\delta x)}{2\delta x} \tag{17}$$

$$\frac{d\boldsymbol{u}_f}{dy} \approx \frac{\boldsymbol{u}_f(y+\delta y) - \boldsymbol{u}_f(x-\delta y)}{2\delta y} \tag{18}$$

$$\frac{d\boldsymbol{u}_f}{dt} \approx \frac{\boldsymbol{u}_f(x+\delta t) - \boldsymbol{u}_f(x-\delta t)}{2\delta t}. \tag{19}$$

We set $\delta x = \delta y$ to half the grid spacing. Parcels only loads in two time instances of the fluid field in memory. The time derivative is always calculated between these two time instances, and thus is constant between field instances. To make sure we never overstep the time instances loaded into memory, we use a timestep of $\delta t = 1/2 dt$, with dt the numerical integration timestep of the simulation. We use a forward derivative when calculating the first step of the RK4 scheme and a backward derivative when calculating the fourth step of the RK4 scheme. As the time derivative is constant between two time instances of the field, this does not affect its value. The numerical integration timestep was set such that the particle samples the velocity grid accurately and the MRG equations are numerically stable. This resulted in a timestep of $dt = 10$ s for advection with the MRG equations and a timestep of $dt = 5$ min for advection with the SM-MRG equation.

For the MRG equations, we need a different scheme as they are of the form:

$$\frac{d\boldsymbol{x}_p}{dt} = \boldsymbol{u}_p(\boldsymbol{x}_p, t) \tag{20}$$

$$\frac{d\boldsymbol{u}_p}{dt} = \boldsymbol{a}_p(\boldsymbol{x}_p, \boldsymbol{u}_p, \boldsymbol{u}_f, t). \tag{21}$$

The acceleration $\boldsymbol{a}_p$ is in our case given by the right-hand side of Eq. (3) and thus depends on both the position and the velocity of the particle. This velocity dependence puts a restriction on the type of algorithms we can use. We need an algorithm that calculates the acceleration at $t + dt$ using the velocity at an earlier timestep t. We solve the full MRG equations using a RK4 scheme adjusted for 2nd order differential equation (Gould et al., 2007). To simplify the notation we introduce index i for the number of timesteps taken ($t = i dt$) and we write $u_p(t)$ as v_i. Using this notation the algorithm is given by:

$$v_{i+1} = v_i + \frac{1}{6}(a_1 + 2a_2 + 2a_3 + a_4) dt \tag{22}$$

$$x_{i+1} = x_i + \frac{1}{6}(v_1 + 2v_2 + 2v_3 + v_4) dt \tag{23}$$

with

$$a_1 = a(x_i, v_i, t_i), \qquad\qquad v_1 = v_i, \tag{24}$$

$$a_2 = a\left(x_i + \frac{v_1}{2}dt, v_i + \frac{a_1}{2}dt, t_i + \frac{1}{2}dt\right), \qquad\qquad v_2 = v_i + \frac{a_1}{2}dt, \tag{25}$$

$$a_3 = a\left(x_i + \frac{v_2}{2}dt, v_i + \frac{a_2}{2}dt, t_i + \frac{1}{2}dt\right), \qquad\qquad v_3 = v_i + \frac{a_2}{2}dt, \tag{26}$$

$$a_4 = a\left(x_i + v_3 dt, v_i + a_3 dt, t_i + dt\right)dt, \qquad\qquad v_4 = v_i + a_3 dt. \tag{27}$$

3.2 Setup particle simulations

The MRG equations depend on the particle diameter and buoyancy. We use spherical "macroplastic" particles with diameter
$d = 25$ cm and buoyancy of $B = 0.68$. We initialize particles evenly over the surface of the ocean in the simulation domain
using a hexagonal grid, where the particles are placed approximately 6.45 km apart. Particles are released a distance $0.5°$
away from the edges of the simulation domain to make sure that the derivatives can be calculated. This resulted in a release of
$N_p = 52,511$ particles.

To prevent stuck particles at the coast, we used a displacement function in our Lagrangian simulations. When the particles
come within 1 grid cell from the coast, they are displaced normal to the coast over a distance of $1\,\mathrm{m/s} \cdot \mathrm{dt}$, with dt the simulation
timestep. When particles come within a distance $\delta x = 1/72°$ from the edge of the simulation domain, they are deleted.

In our simulations, we used 3 different "types" of particles: (i) tracer particles (ii) MRG particles and (iii) SM-MRG particles.
The tracer particles are advected using the standard tracer equation. The MRG particles are advected with the MRG equations
and the SM-MRG particles are advected using the SM-MRG equation. All particles are initialized on the hexagonal grid as
described above.

We performed two types of simulations: (i) short simulations to test settings and (ii) longer simulations to investigate the
effects of the MRG equations on the trajectory of macroplastics. In both simulations, we released all particles at the same time.
For the short simulations, we simulated the particles for 48 hours starting on the 1st of September 2023 at 00:00:00. We used
a simulation timestep of $dt = 10$ s and saved the particle position and slip velocity every 5 min. These simulations are used to
explore the particle Reynolds number, the magnitude of the history term and the difference between advecting particles with
the MRG equations and the SM-MRG equation.

To examine the effect of the MRG equations on the trajectory of macroplastic we perform "long" simulations. In these
simulations, we released particles at 00:00:00 on the first day of each month and simulated their trajectory for 30 days. We
used a simulation timestep of $dt = 5$ min and saved the particle position every output timestep of $\Delta t = 1$ h. We repeated this
simulation for the first of every month for half a year starting from September 1st, 2023.

3.3 Analysis Methods

To quantify the difference in trajectories of different types of particles, we use 3 ensemble averaged measures: (i) The trajectory
length difference, (ii) the relative distance and (iii) the skill score.

For the trajectory length difference, we denote the total amount of output timesteps Δt in simulation period T by M, *i.e.*, $T = M\Delta t$. Using this, we can write the trajectory length after a period T of a single particle n of type α as

$$L_n^\alpha(T) = \sum_{i=2}^{M} |\boldsymbol{x}_n^\alpha(i\Delta t) - \boldsymbol{x}_n^\alpha((i-1)\Delta t)|. \tag{28}$$

The trajectory length difference between particle type α and β, starting at the same location labeled by n, is then defined as $\Delta L_n(T) = L_n^\alpha(T) - L_n^\beta(T)$. In the results, we show the probability distribution function (PDF) over the entire ensemble to show the spread of the data.

The relative distance between a particle of type α and type β, whose starting position is labeled by n, at timestep $t = i\Delta t$ is calculated using

$$D_n^{\alpha-\beta}(t) = |\boldsymbol{x}_n^\alpha(i\Delta t) - \boldsymbol{x}_n^\beta(i\Delta t)|. \tag{29}$$

In the results section we report $\langle D_n^{\alpha-\beta}(t) \rangle_p = 1/N_p \sum_{n=1}^{N_p} D_n^{\alpha-\beta}(t)$, the relative distance averaged over the entire particle ensemble as function of time.

The skill score is a measure of how much trajectories of different type of particles are alike. It was introduced by Liu and Weisberg (2011) as a way to quantify how well observed trajectories are captured by simulated trajectories. We use it to quantify whether particles of type α and type β are significantly different or not. The skill score at timestep $T = M\Delta t$ of particle n is defined as

$$sc(T)_n = \begin{cases} 1 - s_n(T), & \text{if } s(M) \leq 1 \\ 0, & \text{otherwise} \end{cases} \tag{30}$$

with $s_n(T) = \dfrac{\sum_i^M D_n^{\alpha-\beta}(i\Delta t)}{\sum_i^M L_n^\alpha(i\Delta t)}$.

4 Results

4.1 Drag correction factor

To investigate the typical values of the drag correction factor, we performed several test simulations with MRG particles where we varied the drag correction factor. Often in fluid dynamics it is assumed that particles within a certain particle Reynolds number regime have a certain fixed drag correction factor. Here, we refer to this fixed drag correction factor as $c(\mathrm{Re}_p^{\mathrm{In}})$ with $\mathrm{Re}_p^{\mathrm{In}}$ the value used to calculate the correction factor according to Eq. (6). We measured the slip velocity during the simulation, and from this slip velocity we calculated the "measured Reynolds number" $\mathrm{Re}_p^{\mathrm{M}}$. We averaged the measured Reynolds number over all particles and over all timesteps. In Fig. 1(a) we show $\langle \mathrm{Re}_p^{\mathrm{M}} \rangle$ as function of the $c(\mathrm{Re}_p^{\mathrm{In}})$. If we take the ensemble average, we find that the product $c(\mathrm{Re}_p^{\mathrm{In}})\langle \mathrm{Re}_p^{\mathrm{M}} \rangle$ is constant. This can intuitively be understood from the SM-MRG equation (Eq. 16). This equation can be rewritten as

$$\mathrm{Re}_p^{\mathrm{M}} = \frac{1}{c(\mathrm{Re}_p^{\mathrm{In}})} \left(\frac{\tau_s d}{\nu} \frac{2(1-B)}{1+2B} \left| \frac{D\boldsymbol{u}_f}{Dt} + \boldsymbol{f} \times \boldsymbol{u}_f \right| \right).$$
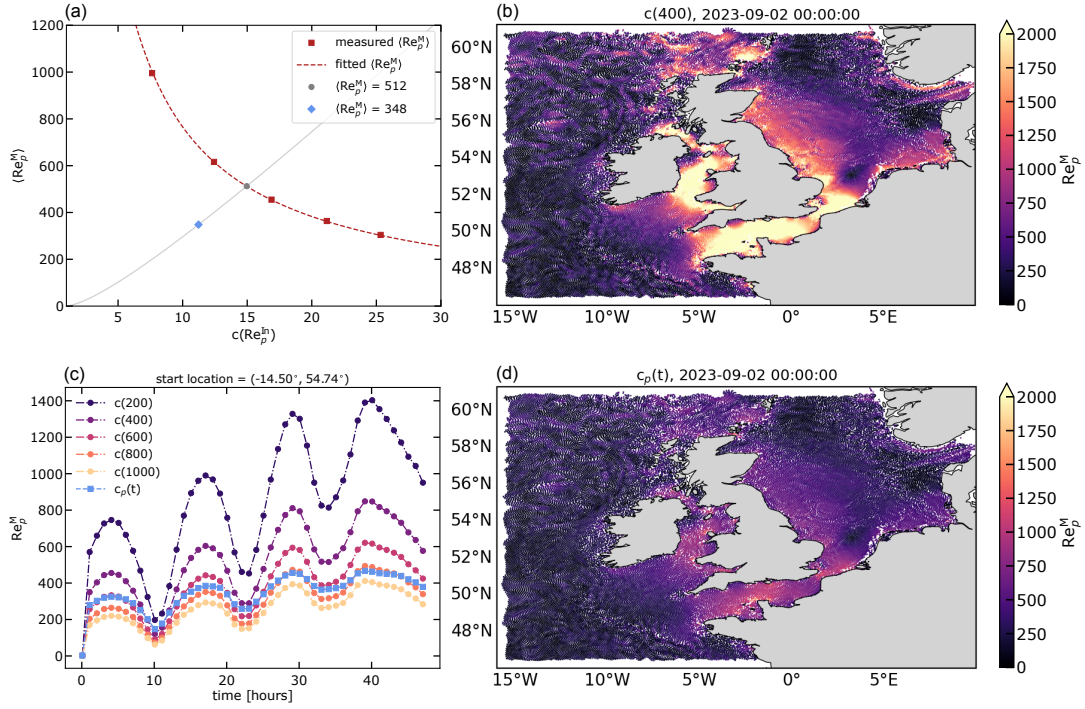
Figure 1. Particle Reynolds numbers in simulations. (a) The ensemble-averaged measured particle Reynolds number $\langle \mathrm{Re}_p^M \rangle$ as function of the drag correction factor $c(\mathrm{Re}_p^{In})$. The data measured in the simulations is shown by the red squares. The plot is zoomed in, and thus the point at $c(0) = 1$ corresponding to $\langle \mathrm{Re}_p^M \rangle = 5904$ is not shown. The data is plotted together with the relation given in Eq. (31) (red dashed line). From this relation we find $c(\mathrm{Re}_p^{In} = 512) = 15$ (grey point). The blue diamond shows $\langle \mathrm{Re}_p^M \rangle = 326$ for a simulation where the Reynolds number is adjusted on the fly. The grey line shows $(c(\mathrm{Re}_p), \mathrm{Re}_p)$. (b) Scatter plot of MRG particles after 12 hours with a fixed drag correction factor of $c(400) = 12$, the particles are colored according to their $\mathrm{Re}_p^M(t)$. (c) $\mathrm{Re}_p^M(t)$ for a particle starting at (14.50° W, 54.74° N) for $c(200)$ up to $c(1000)$ and a $c_p(t)$ that is adjusted on the fly. (d) Scatter plot of MRG particles after 12 hours with a flexible drag correction factor $c_p(t)$, the particles are colored according to their $\mathrm{Re}_p^M(t)$.

The term in brackets only depends on fixed particle properties and characteristics of the flow field and not on the particle Reynolds number and drag correction factor. Thus, if we sample the entire flow field by taking the ensemble average, we find a constant value for the term in the brackets. This means that if we measure a reference value $r = c(\mathrm{Re}_p^{In,ref}) \langle \mathrm{Re}_p^{M,ref} \rangle$ we can find any value of Re_p^M using

$$\langle \mathrm{Re}_p^M \rangle = \frac{r}{c(\mathrm{Re}_p^{In})}. \tag{31}$$

We show this relation as a dashed line in Fig. 1(a). From this relation we find $\mathrm{Re}_p^{In} = \mathrm{Re}_p^M$ (gray line in the plot) for $c(512) = 15$ for particles advected with the MRG equations. These average values indicate that the system is beyond the Stokes regime. This ensemble-averaged particle Reynolds number does not capture the variation in space and time present in the data. In Fig 1(b) we plot the simulated particles after 24 hours, colored according to their measured particle Reynolds number, where we used

$c(400)$. We see that the measured Reynolds number largely varies in space, observing the highest values on the continental shelf where the currents are the strongest due to the tides. In Fig 1(c), we show the measured particle Reynolds number for a single particle over time for different values of $c(\mathrm{Re}_p^{\mathrm{In}})$. The signals have the inertial oscillations clearly imprinted on them. We see that the temporal variance of $\mathrm{Re}_p^{\mathrm{M}}$ is bigger for lower $c(\mathrm{Re}_p^{\mathrm{In}})$. We do not show the data for $c(0)$ as the measured Reynolds

335 number for these settings is much larger than the other curves.

Based on the large variations of the measured particle Reynolds numbers in space and time, we additionally performed simulations where we vary the drag correction function for each particle on the fly. $c_p(t)$ is calculated based on the instantaneous Re_p of the particle at time t. This results in an average measured particle Reynolds number of $\langle \mathrm{Re}_p^{\mathrm{M}} \rangle = 326$, lower than the value predicted by the simulations with constant $c(\mathrm{Re}_p^{\mathrm{In}})$ but still beyond the Stokes regime. In Fig. 1(c) we plot $\mathrm{Re}_p^{\mathrm{M}}$ of the

340 same particle and see that the maxima of the simulations with $c_p(t)$ are damped compared to the constant $c(\mathrm{Re}_p^{\mathrm{In}})$ simulations. In Fig. 1(d) we show the simulated particles after 24 hours, colored according to their $\mathrm{Re}_p^{\mathrm{M}}$ value. Compared to Fig 1(b), the maxima in $\mathrm{Re}_p^{\mathrm{M}}$ for the flexible $c_p(t)$ are damped. In the rest of the result section, we explore both constant drag correction factors and flexible drag correction factors. We expect that flexible drag correction factors better capture reality, as the drag force a particle experiences depends on the particle boundary layer. The timescale of this particle boundary layer is much less

345 than the typical oceanographic timescales, and thus the particle boundary layer changes over time resulting in a drag force regime that changes over time. However, performing simulations with a flexible $c_p(t)$ is numerically more expensive, as a sudden increase in the flow around the particle will result in a large drag force and thus requires small numerical timesteps to keep the simulation stable. For simulations with the MRG equations with a flexible $c_p(t)$ we need a timestep of dt$= 5$ s to keep the simulation stable, while for constant $c(\mathrm{Re}_p^{\mathrm{In}})$ we can use a a timestep of $dt = 5$ min.

4.2 History Force

350

To estimate the importance of the history force, we measure the particle slip velocities in simulations. Using these slip velocities, we estimate the magnitude of the history force without implementing its effect. We took this approach, as more research is needed on the full functional form of the history term for macroscopic objects with $B < 1$. Thus, the value of the history force computed here is not the actual value. In reality, the history force affects the particle velocity and this will change the history

355 force, which is a function of (the derivative of) the particle velocity. The calculation in this section serves purely as an order of magnitude estimation.

We use two different methods to estimate the history term: (i) the Mei/Adrian history kernel and (ii) the Basset kernel integrated over the Oseen time. For the Mei/Adrian history kernel we used the trapezoidal method as proposed by van Hinsberg et al. (2011). This method calculates the history kernel over a preset time window. We explored the effect of the time window

360 and timestep used in the trapezoidal method by calculating the history force for a single particle for a range of timesteps and time windows. In the supplementary information (SI) Fig. S1(a) we show the Mei/Adrian history force as a function of the time window used. We found that a time windows of 20 hours was sufficient to find convergence of the history term (for $c(\mathrm{Re}_p^{\mathrm{In}}) \geq c(10)$). For $c(0)$, the Mei/Adrian kernel reduces to the Basset kernel and no convergence is found within 48 hours. In
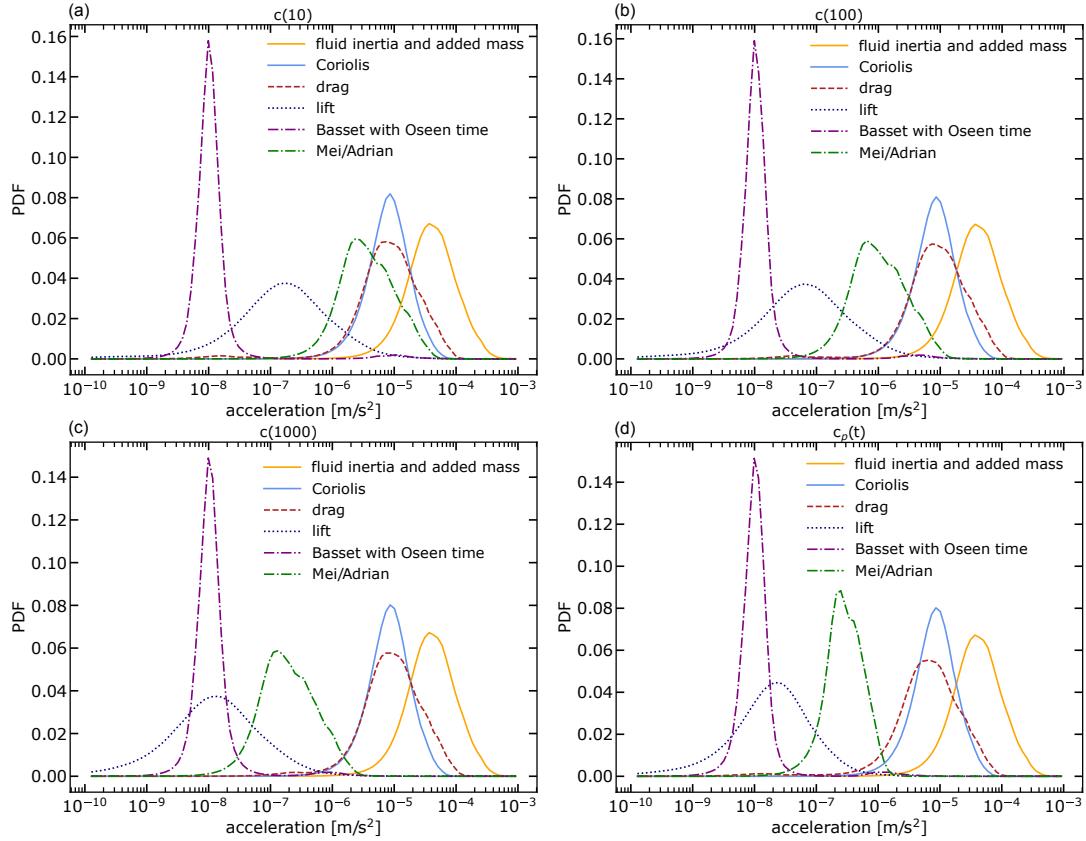
13

Figure 2. Log normal probability distribution functions (PDFs) of acceleration due to the different terms in Eq. (3) where the history term is calculated using either the Basset kernel integrated over the Oseen time (purple line) or using the Mei/Adrian kernel (green line). We show the PDFs for a selection of different drag correction factors: (a) $c(10)$, (b) $c(100)$, (c) $c(1000)$ and (d) $c_p(t)$.

the SI Fig. S1(b), we explore different timesteps in the trapezoidal methods. We find that a timestep of $\Delta t_h = 10$ s is sufficient

365 to calculate the Mei/Adrian history term with the trapezoidal method.

For the Basset history force integrated over the Oseen time, we used a different approach. As slip velocities and their derivatives vary slowly compared to the Oseen time, we use a constant value of the slip velocities and their derivatives to approximate the integral in the history force:

$$\boldsymbol{F}_{\text{history}} = -\frac{3}{2}\rho_f\sqrt{\pi\nu}d^2 \int_{t-t_O}^{t} \frac{1}{\sqrt{t-s}}\left(\frac{d}{ds}(\boldsymbol{u}_f(s) - \boldsymbol{u}_p(s)) + \boldsymbol{f} \times (\boldsymbol{u}_f(s) - \boldsymbol{u}_p(s))\right)ds$$

370
$$\approx -3\rho_f\sqrt{\pi\nu t_O}d^2\left(\frac{d}{dt}(\boldsymbol{u}_p(t) - \boldsymbol{u}_f(t)) + \boldsymbol{f} \times (\boldsymbol{u}_p(t) - \boldsymbol{u}_f(t))\right). \tag{32}$$

We used the full MRG equations to advect particles with $c(0)$, $c(10)$, $c(100)$, $c(1000)$ and a $c_p(t)$ that was adjusted on the fly based on the measured instantaneous Reynolds number of the particle. For the history force, we need to know the

14

temporal derivative of $\boldsymbol{u}_{\text{slip}}$. As the underlying flow velocity field in our simulation is discrete in space and time, the derivative of $\boldsymbol{u}_{\text{slip}}$ is not smooth. As in reality this value is smooth, we fitted $\boldsymbol{u}_{\text{slip}}$ with a cubic polynomial which is twice continuously

375   differentiable.

Using the slip velocity, we calculate the Oseen time. As lower input Reynolds numbers lead to higher slip velocities (*i.e.* the particle velocity increasingly deviates from that of the surrounding fluid velocity) we find the minimum Oseen times for the lowest Reynolds numbers. We find a maximum 95-percentile Oseen time of $t_O^{95\%} = 24$ s for $c(1000)$.

To quantify how important the history force is for the motion of the particle, we compared the magnitude of the acceleration

380   due to the history force in Eq. (3) to the other terms in the equation for $c(10)$, $c(100)$, $c(1000)$, and $c_p(t)$. In Fig. 2, we show the PDFs of the different terms, where we grouped the Coriolis terms outside the history integral together. We find that the acceleration due to the fluid inertia and added mass dominates. Important to note here is that we measure the acceleration of the particle in the Eulerian frame. Du_f/Dt is the forcing that remains if the particle would be a water parcel ($d \to 0$, $B = 1$). We find that the acceleration due to the drag force and Coriolis force have the same order of magnitude. The fluid inertia, drag

385   and Coriolis distribution are very similar for the different values of $c(\text{Re}_p^{\text{In}})$ and $c_p(t)$. The history acceleration calculated with the Mei/Adrian kernel decreases with increasing $c(\text{Re}_p^{\text{In}})$. For the flexible $c_p(t)$ the acceleration due to the Mei/Adrian history force becomes more sharply peaked. For $c(\text{Re}_p^{\text{In}}) \geq c(100)$ and variable $c_p(t)$, the acceleration due to the Mei/Adrian history force is at least an order of magnitude smaller than the acceleration due to the Coriolis and drag term and 2 orders smaller than the acceleration due to the fluid inertia.

390   We find a much smaller value if we calculate acceleration due to the history force using the Basset kernel over the Oseen time. It is on average 3 orders of magnitude smaller than acceleration due to the Coriolis and drag force. The acceleration due to the history force calculated using the Basset kernel with Oseen time is constant for different $c(\text{Re}_p^{\text{In}})$ and $c_p(t)$. This is caused by the balance between the (derivatives of the) slip velocities and Oseen times. At lower $c(\text{Re}_p^{\text{In}})$ the (derivatives of the) slip velocities become larger but the Oseen times become shorter.

395   Recall that while the integral of the Basset kernel over the Oseen time is likely an underestimate for the true history force, because it completely cuts off the contribution from the long-time $1/t^2$-decaying part of the kernel, the full Mei/Adrian history integral is an overestimate, as the Mei/Adrian kernel has the unrealistically delayed transition from the short-time $1/\sqrt{t}$-decay to the long-time $1/t^2$-decay. The truth is thus somewhere between these two estimates. Because Re_p in our case is > 100, and because even the Mei/Adrian history integral is at least an order of magnitude smaller than the other terms in the MRG

400   equation for this parameter regime, we conclude that the history force only plays a secondary role in our system.

4.3   Slow manifold Maxey-Riley-Gatignol equations

For the case where the history term can be ignored, the MRG equations can be simplified to the SM-MRG equations, as explained in section 2.4. In general, the slow manifold limit holds if $\varepsilon/c(\text{Re}_p) = \frac{\tau_s}{c(\text{Re}_p)}\frac{U}{L} \ll 1$. We find a maximum value of $\varepsilon = 0.32$ and a minimum value of $\varepsilon/c(1000) = 0.013$. However, the fluid flow can change faster than the timescale given

405   by L/U. Due to this abrupt change, the solution to the SM-MRG equation can start to diverge from the solutions of the full MRG equations (Haller and Sapsis, 2008). Here, we investigate whether the trajectories simulated with the MRG equations are
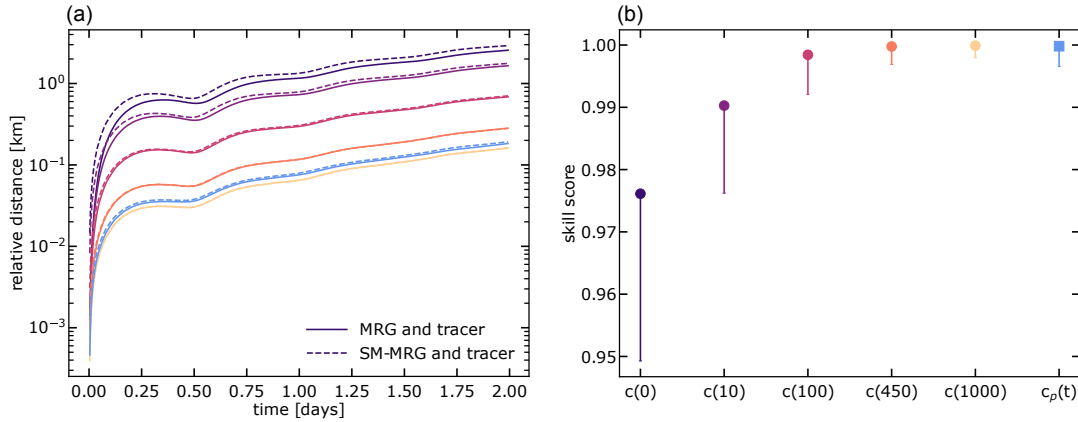
15

Figure 3. Difference between advecting particles with MRG equations or SM-MRG equation. (a) Relative distance between MRG particles and tracer particles (solid lines) and SM-MRG particles and tracer particles (dashed lines) over time. The different colors indicate different values of $c(\mathrm{Re}_p^{\mathrm{In}})$ and $c_p(t)$. The values corresponding to the colors are indicated on the x-axis of panel (b). (b) The skill score (Eq. (30)) of SM-MRG particles compared to MRG particles for different values of $c(\mathrm{Re}_p^{\mathrm{In}})$ and $c_p(t)$. The error bar shows the standard deviation (only shown downward, as the skill score cannot be larger than 1).

similar to the trajectories simulated with the SM-MRG equation. We used $c(0)$, $c(10)$, $c(100)$, $c(450)$, $c(1000)$ and $c_p(t)$. To quantify the difference between the trajectories obtained with the MRG equations and SM-MRG equation, we first compare the difference between the MRG and tracer particles to the difference between SM-MRG and tracer particles. In Fig. 3(a),

410   we plot the relative distance averaged over all particles between MRG and SM-MRG advection and tracer particles. We find that for smaller $c(\mathrm{Re}_p^{\mathrm{In}})$ there is a difference between the relative distance of MRG and full-MRG particles, this difference decreases with increasing $c(\mathrm{Re}_p^{\mathrm{In}})$. For flexible $c_p(t)$ we also observe a difference. To quantify whether the trajectories of the MRG particles and SM-MRG particles are significantly different, we use the skill score as introduced in Eq. (30). We plot the skill score for the different $c(\mathrm{Re}_p^{\mathrm{In}})$ and $c_p(t)$ in Fig. 3(b). In general, we find a skill score above 0.97, showing that the

415   trajectories of the MRG and SM-MRG particles are very similar. We find that, for $c(\mathrm{Re}_p^{\mathrm{In}}) \geq c(100) = 4.9$ and flexible $c_p(t)$, the average values are very close to one and lower bounds of the skill score are > 0.99 and thus the difference between MRG and SM-MRG particle trajectories is negligible.

4.4 Tracer trajectories vs. SM-MRG trajectories

From the sensitivity tests, we find that macroplastics in the NWES are beyond the Stokes regime. Therefore, we choose to per-

420   form simulations for $c(100)$, $c(450)$, $c(1000)$ and flexible $c_p(t)$ for studying the effect on the trajectories of macroplastics. For these values, we ignore the effect of the history term. We found that advecting with the MRG equations or SM-MRG equation for these Reynolds numbers yields very similar trajectories, so we perform all simulations with the SM-MRG equation. We use an integration timestep of $dt = 5$ min. We compare the particles advected with the SM-MRG equation with tracer particles. We use 2 different types of velocity input fields: (a) hourly averaged fields and (b) daily averaged fields.
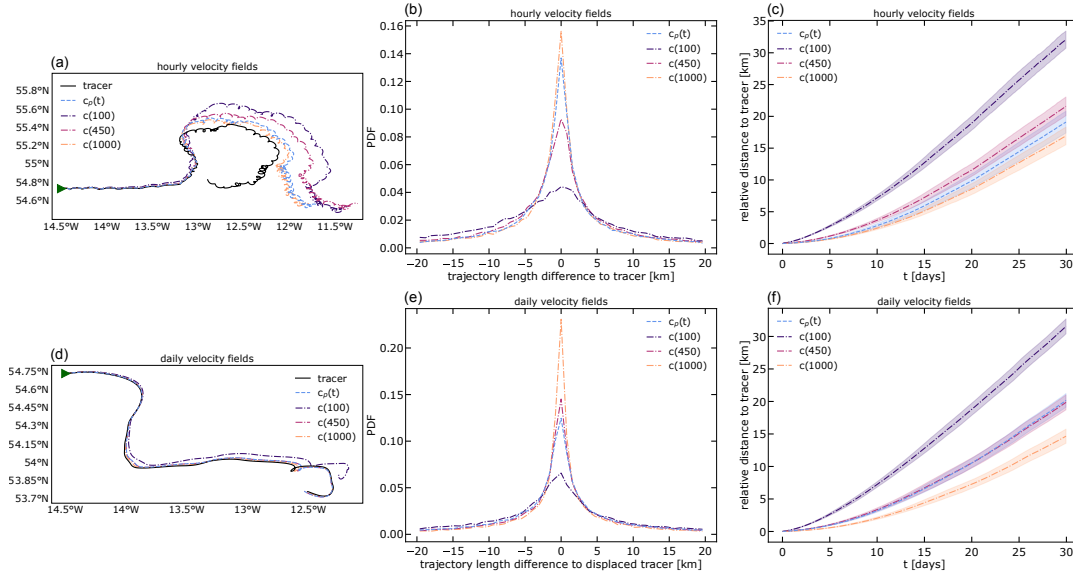
16

Figure 4. Difference between tracer particles and SM-MRG particles for velocity fields with different temporal resolutions. Hourly velocity fields were used in (a)-(c), and daily velocity fields were used in (d)-(f). Panels (a) and (d) show the trajectories of a tracer particle and SM-MRG particles with different $c(\mathrm{Re}_p^{\mathrm{In}})$ and $c_p(t)$, starting at $14.50°$ W, $54.74°$ N on September 1st 2023. Panels (b) and (e) show PDFs of trajectory length difference after 30 days between SM-MRG particles and tracer particles for several different $c(\mathrm{Re}_p^{\mathrm{In}})$ and $c_p(t)$ (see legend). Panels (c) and (f) show relative distance between SM-MRG particles and tracer particles for several different $c(\mathrm{Re}_p^{\mathrm{In}})$ and $c_p(t)$ (see legend). The shaded areas show the standard error of the mean for the simulations started in different months.

425   In Fig. 4(a), we show the trajectories for particles that started at $(14.50°$ W, $54.74°$ N) on September 1st 2023, at 00:00:00 and were simulated for 30 days, using velocity fields with an hourly resolution. Increasing $c(\mathrm{Re}_p^{\mathrm{In}})$ brings the trajectory of the SM-MRG particle closer to the trajectory of the tracer particle.

This is a pattern we also find if we average over all particles in the simulations. In Fig. 4(b) we show the trajectory length difference between SM-MRG particles and tracer particles and in Fig. 4(c) we show the average relative distance between
430   SM-MRG particles and tracer particles for velocity fields with an hourly resolution. We find that the average relative distance for $c(100)$ is significantly larger, with an average relative distance of 32 km after 30 days. The average relative distances for $c(450)$, $c(1000)$ and flexible $c_p(t)$ is small, whereas the average relative distance for SM-MRG particles with flexible $c_p(t)$ falls just in between the curves for $c(450)$ and $c(1000)$. The PDF of the trajectory length difference shows the same trend, where $c(100)$ has the broadest distribution and the distributions become more sharply peaked with increasing $c(\mathrm{Re}_p^{\mathrm{In}})$. The
435   maximum value of the distribution for SM-MRG particles with flexible $c_p(t)$ again lies between $c(450)$ and $c(1000)$.

We find that the trajectories of SM-MRG particles with flexible $c_p(t)$ are sensitive to the temporal resolution of the underlying velocity field. In Fig. 4(d) we show the trajectories for particles that again started at $(14.50°$ W, $54.74°$ N) on September 1st 2023, at 00:00:00 and were simulated for 30 days, but now using velocity fields with a daily resolution. The path the particle takes is different as the particle is not moved by the short-time scale flows and thus samples a different part of the underlying

17

440   velocity field. We clearly see that inertial oscillations in the underlying velocity field are averaged out, resulting in smoother trajectories. In Fig. 4(e) and Fig. 4(f), we show the distribution of the trajectory length difference after 30 days and average relative distance over time for particles advected in a velocity field with a daily temporal resolution. As sub-daily flows are filtered out in the daily velocity field, we expect that the difference in the trajectory length becomes smaller as the field is less dispersive. Indeed, we see that for the daily fields, the distributions with a fixed $c(\mathrm{Re}_p^{\mathrm{In}})$ are more sharply peaked around zero

445   than the distributions of the hourly fields. However, for SM-MRG particles with a flexible $c_p(t)$, we find that the PDF of the trajectory length difference becomes less peaked around zero. The PDF for the hourly velocity fields has a maximum of 0.137, while the PDF for daily velocity fields has a maximum of 0.125. For the average relative distances we observe the same trend. For SM-MRG particles with a fixed $c(\mathrm{Re}_p^{\mathrm{In}})$, the average relative distance after 30 days is slightly smaller in simulations with daily velocity fields than in simulations with hourly velocity fields. For SM-MRG particles with a flexible $c_p(t)$, the average

450   relative distance after 30 days is larger when using daily velocity fields than when using hourly fields. Due to the difference in trends $c(\mathrm{Re}_p^{\mathrm{In}})$ and or flexible $c_p(t)$ between daily and hourly fields, the sequence of the curves is different for the daily velocity fields. The peak of the trajectory length difference for flexible $c_p(t)$ now lies just below the peak of $c(450)$ and the curve of the relative distance over time lies just above $c(450)$.

      Finally, we investigate in more detail how the constituents of the SM-MRG equation affects the trajectories. In the 2D

455   SM-MRG equation without history term there are two forcings that can make the trajectory of a particle different from tracer particles. These are (i) the forcing associated with the Coriolis effect (terms scaling with $\boldsymbol{f}$) and (ii) the forcing associated with the spatial and temporal gradients in the underlying velocity field (terms scaling with $D\boldsymbol{u}_f/Dt$). We use simulations to investigate their effects separately. We perform one series of simulations where we only include gradient effects (setting the terms associated with the Coriolis force to zero) and one series of simulations with only Coriolis effects (setting the terms

460   associated with the spatial and temporal gradients in the velocity field to zero). We used the hourly velocity field with the same range of $c(\mathrm{Re}_p^{\mathrm{In}})$ as before and flexible $c_p(t)$.

      In Fig. 5(a), we show the trajectories for particles that started at $(14.50°\,\mathrm{W}, 54.74°\,\mathrm{N})$ on September 1st 2023, at 00:00:00 and were simulated for 30 days. For the SM-MRG particles we show the trajectories for flexible $c_p(t)$. The trajectory of the particle forced with the Coriolis force is different from the tracer particle, while the particle forced with only the gradients in

465   the velocity fields has a very similar trajectory as the tracer particle.

      This pattern is also observed when we average over all particles in the simulations. Fig. 5(b) and Fig. 5(d) show the trajectory length difference and Fig. 5(c) and Fig. 5(e) show the relative distance between the SM-MRG particles and tracer particles. In Fig. 5(b) and Fig. 5(c) we only included Coriolis forcing, and in Fig. 5(d) and Fig. 5(e) we only included gradient forcing. It can clearly be seen that the forcing associated with the Coriolis effects are the main driver for the difference between MRG
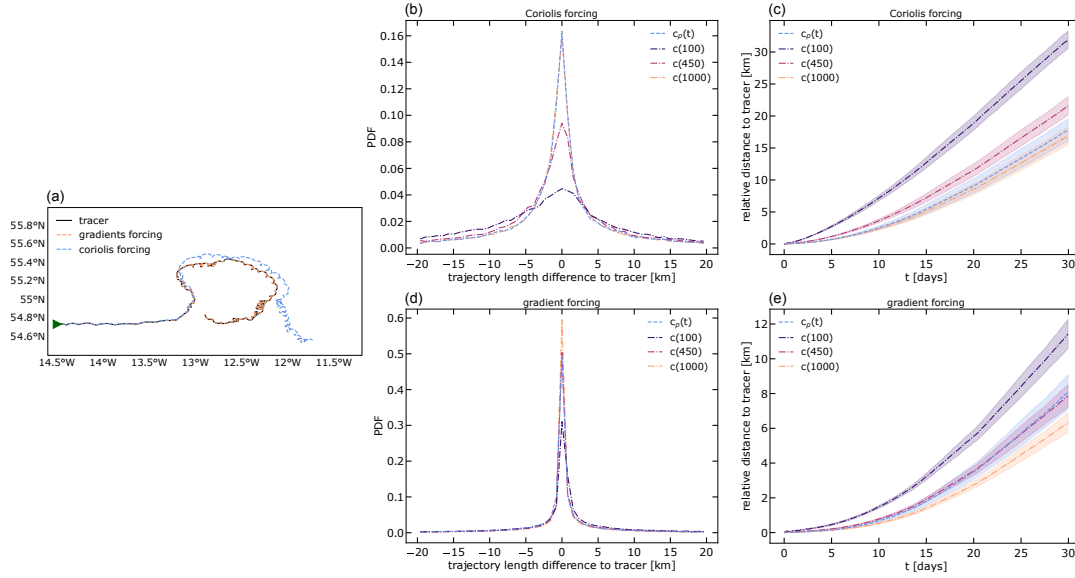
470   particles and tracer particles.

Figure 5. Difference between tracer particles and SM-MRG particles that are forced with Coriolis forces or gradient forces. (a) Trajectories of a tracer particle and SM-MRG particles forced with either Coriolis terms or spatiotemporal gradients in the velocity field. The particles started at $14.50°$ W, $54.74°$ N on September 1st 2023 and both the SM-MRG particles had a flexible $c_p(t)$. In panels (b) and (c) the SM-MRG particles are forced with Coriolis terms ($D\boldsymbol{u}_f/Dt$ is set to zero) and in panels (d) and (e) the SM-MRG particles are forced with the gradients in the velocity field ($\boldsymbol{f}$ is set to zero). Panels (b) and (d) show PDFs of trajectory length difference after 30 days between SM-MRG particles and tracer particles for several different $c(\mathrm{Re}_p^{\mathrm{In}})$ and $c_p(t)$ (see legend). Panels (c) and (e) show the relative distance between SM-MRG particles and tracer particles for several different $c(\mathrm{Re}_p^{\mathrm{In}})$ and $c_p(t)$ (see legend). The shaded areas show the standard error of the mean for the simulations started in different months.

5   Discussion and conclusions

We investigated a number of aspects of the simulation of macroplastic trajectories in the NWES with the Maxey-Riley-Gatignol equations. We found that we need to account for the fact that the particles have a particle Reynolds number Re_p beyond the Stokes regime. We do so by using a drag force with a drag correction factor that is a function of the $c(\mathrm{Re}_p)$. We find that the

475   Re_p for the macroplastics we studied in the NWES, is on average around 450. However, we find that as the underlying flow varies in space and time, so does the Re_p. Thus, we implemented a flexible $c_p(t)$ that is calculated on the fly in simulations. We find that for the Reynolds number regime of macroplastics in the NWES, the history term is at least an order of magnitude smaller than other forces acting on the particle. Also, the trajectories of the particles are well captured with the slow manifold MRG equation, which further simplifies the simulations. Using these equations to simulate the trajectories of macroplastics

480   in the NWES, we find that increasing the drag correction factor $c(\mathrm{Re}_p^{\mathrm{In}})$ makes the particles more flow following, and that and the particles with a flexible $c_p(t)$ behave similar to tracer particles (due to their large variable Re_p). We find that the observed differences between the macroplastic trajectories and tracer trajectories are mainly due to the forcing associated with

19

the Coriolis effects in the slow manifold (SM-MRG) equation, while the forcing associated with gradients in the velocity fields has only a minor effect.

485   An important result of this study is that the behavior of particles simulated with the MRG equations with a flexible $c_p(t)$ is affected by the temporal resolution of the underlying velocity field. We observe an unexpected trend when using a velocity field with a coarser temporal resolution. A daily field has fewer short-time variability that can lead to dispersion of the particle, thus one expect that the tracer particles and the SM-MRG particles to become more similar, which we indeed observe for constant $c(\mathrm{Re}_p^{\mathrm{In}})$. However, for the flexible $c_p(t)$ we find that the difference between the tracer particles and MRG-particles is larger

490 using daily fields than using hourly fields. This is because fields with a coarser time resolution average out variations in the velocity field, *e.g.*, daily fields average out tidal currents. Without these extreme values, the slip velocity a particle experiences decreases, and thus $c_p(t)$ is underestimated, resulting in an underestimation of the drag force. In addition, there will be pre-existing turbulence in the ocean on the small scale due to for example breaking waves. This pre-existing turbulence would lead to a higher Reynolds number regime (larger value of $c_p(t)$) and thus the drag force in reality will be larger.

495   This means that one should take care when implementing the MRG equation with flexible $c_p(t)$ as used in this paper. Even the high-resolution field used here is still averaged over 1 hour. In addition, small scale features of the flow are not resolved due to the finite spatial resolution. Thus, the variations in the velocity will be even higher in the real NWES, which most likely results in larger values for $c_p(t)$ and thus particles that are more flow-following.

    In addition, the particle slip velocity will be affected by the windage, which we ignored in this study. In reality, buoyant

500 particles will not only experience a drag force due to the ocean currents but also due to the wind as they partly stick out of the surface. In general, the wind and ocean currents are not aligned in a tidal region like the NWES, and thus the slip velocity of the particle with the ocean current will increase under the influence of the wind. This will lead to a higher $c_p(t)$ for the ocean drag force. Likewise, the drag force on the particle due to the wind will depend on the Re_p of the air, which will be influenced by the ocean current drag as this increases the slip velocity of the particle with the wind, increasing the air Re_p.

505   We thus expect that in reality the drag correction factor is even larger than found in the simulations with hourly velocity fields, and thus the particle trajectory will be completely dominated by the drag forces of the wind and ocean currents (including Stokes drift). Hence, instead of using the flexible $c_p(t)$ SM-MRG equation, we think an adjusted leeway-type formulation would be most suited to simulate macroplastics in the NWES. For this, the derivation of Beron-Vera et al. (2019) has to be extended for nonzero Re_p that can be different in air and in water. This might result in a windage factor that is dependent on the

510 relative strength of the ocean currents and the wind. How exactly the windage term scales with the relative state of the ocean surface current and wind, has to be carefully examined in future work.

Code availability. The code for the Lagrangian simulations and analysis is available via https://github.com/Parcels-code/Maxey_Riley_ advection

References

AlAli, O., Tarver, B., and Coimbra, C. F. M.: Particle response to oscillatory flows at finite Reynolds numbers, Physics of Fluids, 36, 103 367, https://doi.org/10.1063/5.0229970, 2024.

Beron-Vera, F. J. and Miron, P.: A minimal Maxey–Riley model for the drift of Sargassum rafts, Journal of Fluid Mechanics, 904, A8, https://doi.org/10.1017/jfm.2020.666, 2020.

Beron-Vera, F. J., Olascoaga, M. J., and Miron, P.: Building a Maxey–Riley framework for surface ocean inertial particle dynamics, Physics of Fluids, 31, 2019.

Bonner, G., Beron-Vera, F. J., and Olascoaga, M. J.: Charting the course of Sargassum: Incorporating nonlinear elastic interactions and life cycles in the Maxey–Riley model, PNAS Nexus, 3, pgae451, https://doi.org/10.1093/pnasnexus/pgae451, 2024.

Breivik, Ø., Allen, A. A., Maisondieu, C., and Roth, J. C.: Wind-induced drift of objects at sea: The leeway field method, Applied Ocean Research, 33, 100–109, https://doi.org/https://doi.org/10.1016/j.apor.2011.01.005, 2011.

Daitche, A.: On the role of the history force for inertial particles in turbulence, Journal of Fluid Mechanics, 782, 567–593, https://doi.org/10.1017/jfm.2015.551, 2015.

Delandmeter, P. and van Sebille, E.: The Parcels v2.0 Lagrangian framework: new field interpolation schemes, Geoscientific Model Development, 12, 3571–3584, https://doi.org/10.5194/gmd-12-3571-2019, 2019.

Dey, S., Ali, S. Z., and Padhi, E.: Terminal fall velocity: the legacy of Stokes from the perspective of fluvial hydraulics, Proceedings of the Royal Society A, 475, 20190 277, 2019.

Dorgan, A. J. and Loth, E.: Efficient calculation of the history force at finite Reynolds numbers, International journal of multiphase flow, 33, 833–848, 2007.

Eriksen, M., Lebreton, L. C. M., Carson, H. S., Thiel, M., Moore, C. J., Borerro, J. C., Galgani, F., Ryan, P. G., and Reisser, J.: Plastic Pollution in the World's Oceans: More than 5 Trillion Plastic Pieces Weighing over 250,000 Tons Afloat at Sea, PLOS ONE, 9, 1–15, https://doi.org/10.1371/journal.pone.0111913, 2014.

Farazmand, M. and Haller, G.: The Maxey–Riley equation: Existence, uniqueness and regularity of solutions, Nonlinear Analysis: Real World Applications, 22, 98–106, https://doi.org/https://doi.org/10.1016/j.nonrwa.2014.08.002, 2015.

Gatignol, R.: The Faxén formulae for a rigid particle in an unsteady non-uniform Stokes flow, Journal De Mecanique Theorique Et Appliquee, 2, 143–160, 1983.

Gould, H., Tobochnik, J., and Christian, W.: Simulating Particle Motion, pp. 47–87, H. Gould, J. Tobochnik, W. Christian, 3rd edn., 2007.

Haller, G. and Sapsis, T.: Where do inertial particles go in fluid flows?, Physica D: Nonlinear Phenomena, 237, 573–583, https://doi.org/https://doi.org/10.1016/j.physd.2007.09.027, 2008.

Jaganathan, D., Prasath, S. G., Govindarajan, R., and Vasan, V.: The Basset–Boussinesq history force: its neglect, validity, and recent numerical developments, Frontiers in Physics, 11, https://doi.org/10.3389/fphy.2023.1167338, 2023.

Kaandorp, M. L., Lobelle, D., Kehl, C., Dijkstra, H. A., and van Sebille, E.: Global mass of buoyant marine plastics dominated by large long-lived debris, Nature Geoscience, 16, 689–694, 2023.

Kim, I., Elghobashi, S., and Sirignano, W. A.: On the equation for spherical-particle motion: effect of Reynolds and acceleration numbers, Journal of Fluid Mechanics, 367, 221–253, 1998.

Langlois, G. P., Farazmand, M., and Haller, G.: Asymptotic Dynamics of Inertial Particles with Memory, Journal of Nonlinear Science, 25, 1225–1255, https://doi.org/10.1007/s00332-015-9250-0, 2015.

Le Moigne, M., Brun, M., Gerigny, O., and Galgani, F.: Tackling Marine Litter in the Atlantic Area. Spatial and temporal variability in floating litter in North Sea / English Channel and Bay of Biscay / Celtic Sea - 2015-2020, Report, CleanAtlantic, https://archimer.ifremer.fr/doc/00750/86159/, 2021.

560   Lebreton, L. C. M., Greer, S. D., and Borrero, J. C.: Numerical modelling of floating debris in the world's oceans, Marine Pollution Bulletin, 64, 653–661, https://doi.org/https://doi.org/10.1016/j.marpolbul.2011.10.027, 2012.

Liu, Y. and Weisberg, R. H.: Evaluation of trajectory modeling in different dynamic regions using normalized cumulative Lagrangian separation, Journal of Geophysical Research: Oceans, 116, https://doi.org/https://doi.org/10.1029/2010JC006837, 2011.

Liubartseva, S., Coppini, G., Lecci, R., and Clementi, E.: Tracking plastics in the Mediterranean: 2D Lagrangian model, Marine Pollution

565   Bulletin, 129, 151–162, https://doi.org/https://doi.org/10.1016/j.marpolbul.2018.02.019, 2018.

Lovalenti, P. M. and Brady, J. F.: The hydrodynamic force on a rigid particle undergoing arbitrary time-dependent motion at small Reynolds number, Journal of Fluid Mechanics, 256, 561–605, https://doi.org/10.1017/S0022112093002885, 1993.

Maxey, M. R. and Riley, J. J.: Equation of motion for a small rigid sphere in a nonuniform flow, The Physics of Fluids, 26, 883–889, https://doi.org/10.1063/1.864230, 1983.

570   Maximenko, N., Hafner, J., Kamachi, M., and MacFadyen, A.: Numerical simulations of debris drift from the Great Japan Tsunami of 2011 and their verification with observational reports, Marine Pollution Bulletin, 132, 5–25, https://doi.org/https://doi.org/10.1016/j.marpolbul.2018.03.056, 2018.

Mei, R. and Adrian, R. J.: Flow past a sphere with an oscillation in the free-stream velocity and unsteady drag at finite Reynolds number, Journal of Fluid Mechanics, 237, 323–341, 1992.

575   Mei, R., Lawrence, C. J., and Adrian, R. J.: Unsteady drag on a sphere at finite Reynolds number with small fluctuations in the free-stream velocity, Journal of Fluid Mechanics, 233, 613–631, https://doi.org/10.1017/S0022112091000629, 1991.

Morales-Caselles, C., Viejo, J., Martí, E., González-Fernández, D., Pragnell-Raasch, H., González-Gordillo, J. I., Montero, E., Arroyo, G. M., Hanke, G., Salvo, V. S., et al.: An inshore–offshore sorting system revealed from global classification of ocean litter, Nature Sustainability, 4, 484–493, https://doi.org/10.1038/s41893-021-00720-8, 2021.

580   Moreno-Casas, P. A. and Bombardelli, F. A.: Computation of the Basset force: recent advances and environmental flow applications, Environmental Fluid Mechanics, 16, 193–208, 2016.

Prasath, S. G., Vasan, V., and Govindarajan, R.: Accurate solution method for the Maxey–Riley equation, and the effects of Basset history, Journal of Fluid Mechanics, 868, 428–460, https://doi.org/10.1017/jfm.2019.194, 2019.

Ricker, M. and Stanev, E. V.: Circulation of the European northwest shelf: a Lagrangian perspective, Ocean Science, 16, 637–655,

585   https://doi.org/10.5194/os-16-637-2020, 2020.

Rypina, I. I., Pratt, L. J., and Dotzel, M.: Aggregation of slightly buoyant microplastics in 3D vortex flows, Nonlinear Processes in Geophysics, 31, 25–44, https://doi.org/10.5194/npg-31-25-2024, 2024.

Sano, T.: Unsteady flow past a sphere at low Reynolds number, Journal of Fluid Mechanics, 112, 433–441, https://doi.org/10.1017/S0022112081000499, 1981.

590   Sharqawy, M. H., Lienhard, J. H., and Zubair, S. M.: Thermophysical properties of seawater: a review of existing correlations and data, Desalination and Water Treatment, 16, 354–380, https://doi.org/https://doi.org/10.5004/dwt.2010.1079, 2010.

Soto-Navarro, J., Jordá, G., Deudero, S., Alomar, C., Amores, Á., and Compa, M.: 3D hotspots of marine litter in the Mediterranean: A modeling study, Marine Pollution Bulletin, 155, 111 159, https://doi.org/https://doi.org/10.1016/j.marpolbul.2020.111159, 2020.

Sunberg, L. K. C., DiBenedetto, M. H., Ouellette, N. T., and Koseff, J. R.: Parametric study of the dispersion of inertial ellipsoidal particles
595   in a wave-current flow, Physical Review Fluids, 9, 034 302, 2024.

Tanga, P., Babiano, A., Dubrulle, B., and Provenzale, A.: Forming Planetesimals in Vortices, Icarus, 121, 158–170,
       https://doi.org/https://doi.org/10.1006/icar.1996.0076, 1996.

Tekman, M. B., Gutow, L., and Bergmann, M.: Marine Debris Floating in Arctic and Temperate Northeast Atlantic Waters, Frontiers in
       Marine Science, 9, https://doi.org/10.3389/fmars.2022.933768, 2022.

600 Turrell, W. R.: Spatial distribution of foreshore litter on the northwest European continental shelf, Marine Pollution Bulletin, 142, 583–594,
       https://doi.org/https://doi.org/10.1016/j.marpolbul.2019.04.009, 2019.

Urizarna-Carasa, J., Ruprecht, D., von Kameke, A., and Padberg-Gehle, K.: Relevance of the Basset history term for Lagrangian particle
       dynamics, Chaos: An Interdisciplinary Journal of Nonlinear Science, 35, 073 122, https://doi.org/10.1063/5.0225926, 2025.

van Hinsberg, M. A. T., ten Thije Boonkkamp, J. H. M., and Clercx, H. J. H.: An efficient, second order method for the approximation of the
605   Basset history force, Journal of Computational Physics, 230, 1465–1478, 2011.

Wakaba, L. and Balachandar, S.: On the added mass force at finite Reynolds and acceleration numbers, Theoretical and Computational Fluid
       Dynamics, 21, 147–153, https://doi.org/10.1007/s00162-007-0042-5, 2007.

White, F. M.: Solutions of the Newtonian Viscous-Flow Equations, in: Viscous Fluid Flow. 2nd Edition, p. 182, McGraw-Hill, 1991.

Wienders, N.: STOKES DRIFTER, 2021.